

Fast and cheap approximation of Green function uncertainty for waveform-based earthquake source inversions

M. Hallo and F. Gallovič

Faculty of Mathematics and Physics, Charles University, Prague, Czech Republic. E-mail: hallo@karel.troja.mff.cuni.cz

Accepted 2016 August 23. Received 2016 June 14; in original form 2016 March 7

SUMMARY

Green functions (GFs) are an essential ingredient in waveform-based earthquake source inversions. Hence, the error due to imprecise knowledge of a crustal velocity model is one of the major sources of uncertainty of the inferred earthquake source parameters. Recent strategies in Bayesian waveform inversions rely on statistical description of the GF uncertainty by means of a Gaussian distribution characterized by a covariance matrix. Here we use Monte-Carlo approach to estimate the GF covariance considering randomly perturbed velocity models. We analyse the dependence of the covariance on various parameters (strength of velocity model perturbations, GF frequency content, source-station distance, etc.). Recognizing that the major source of the GF uncertainty is related to the random time shifts of the signal, we propose a simplified approach to obtain approximate covariances, bypassing the numerically expensive Monte-Carlo simulations. The resulting closed-form formulae for the approximate auto-covariances and cross-covariances between stations and components can be easily implemented in existing inversion techniques. We demonstrate that the approximate covariances exhibit very good agreement with the Monte-Carlo estimates, providing realistic variations of the GF waveforms. Furthermore, we show examples of implementation of the covariance matrix in a Bayesian moment tensor inversion using both synthetic and real data sets. We demonstrate that taking the GF uncertainty into account leads to improved estimates of the moment tensor parameters and their uncertainty.

Key words: Inverse theory; Earthquake source observations; Theoretical seismology; Statistical seismology; Wave propagation.

1 INTRODUCTION

Inference of earthquake source parameters is an important subject in seismology. Realistic estimate of the uncertainty of earthquake source inversion results is essential for evaluation of solution quality. Strictly speaking, any geological interpretation of centroid moment tensor or rupture model requires proper assessment of their uncertainty (e.g. Dettmer *et al.* 2014; Duputel *et al.* 2015; Sokos *et al.* 2015). For example, Valentine & Woodhouse (2010) also showed that imprecise source parameters negatively affect seismic tomography models.

In waveform-based earthquake source inversions, two major origins of uncertainty can be recognized. The first one is related to the data error, which may be due to instrumental or ambient noise effects (Mustać & Tkalcic 2016). Typically, when dealing with larger events, the signal-to-noise ratio is rather high and data corrupted by strong disturbances (e.g. Zahradník & Plešinger 2010; Vackář *et al.* 2015) can be omitted. The second source of uncertainty, which is almost always neglected, is related to the uncertainty of Green's functions (GFs) due to the inaccuracy of the crustal model considered. In practical applications, the uncertainties of the inferred

source parameters due to the above-mentioned causes are typically estimated by accepting all models within a given threshold on the misfit value (e.g. Piatanesi *et al.* 2007; Gallovič & Zahradník 2012; Valentine & Trampert 2012; Zahradník & Custódio 2012). However, the value of such threshold is often ad-hoc or ‘empirical’, not based on a proper analysis of the underlying origin of the uncertainty. We point out that imprecise knowledge of the velocity model can lead to spurious non-double-couple components in moment tensor inversions (Zahradník *et al.* 2015) and artificial slip-rate peaks in slip inversions (Gallovič *et al.* 2015).

In terms of the Bayesian inference, the uncertainty of source inversion results can be formulated by posterior probability density function (PDF) of the model parameters (Tarantola 2005, pp. 32–37). In such a case, the two major sources of uncertainty (data error and GFs uncertainty) must be expressed by statistical models, typically by Gaussian PDFs parameterized by mean values and covariances. In particular, Yagi & Fukahata (2011) suggest an iterative inversion approach taking into account the GFs variance (diagonal covariance matrix). The authors, however, consider only an ad-hoc estimate of the variance based on the maximum amplitude of the GFs without a proper justification. Kubo *et al.* (2016)

and Minson *et al.* (2013) also considered diagonal GF covariance matrix in their Bayesian slip inversion, treating the GF variance as an unknown parameter with uniform and log-normal prior PDF, respectively. Duputel *et al.* (2012) show the importance of considering the full covariance matrix of GF in the moment tensor inversion. However, in their examples they assume that the major origin of the error is due to the centroid mislocation. This study has been extended by Duputel *et al.* (2014, 2015), who propose to estimate the full covariance matrix approximately by considering linear relationship between the GFs and random, generally 3-D, perturbations of the velocity model. However, their approach requires evaluation of sensitivity kernels, which are, in practice, very expensive to acquire (e.g. Kubo *et al.* 2016). An alternative approach is represented by ‘empirical’ estimation of the covariances from data residuals in so-called hierarchical inversions (Dettmer *et al.* 2007, 2014; Mustać & Tkalcic 2016). In particular, Dettmer *et al.* (2007, 2014) take into account the non-stationary character of the noise by scaling rows and columns of the covariance matrix by running averages of the residual waveforms.

We point out that not only the inversion procedures taking the GF uncertainty into account but even the methodology for estimation of the GF covariance matrix itself are not sufficiently developed yet. Moreover, besides exact uncertainty estimations, simple and easy-to-implement approaches have to be developed in order to efficiently involve the GF uncertainty in practical source inversions. The primary aim of this paper is to introduce such an approach by means of finding reasonable approximations for efficient evaluation of the GF covariance functions. We also address the estimation of cross-covariances between components at a station and between stations, which have not been discussed in the literature yet despite being essential to correctly account for possible mutual dependencies of the GFs (e.g. Tarantola 2005, pp. 32–37).

In this paper, we first show by means of Monte-Carlo simulations in randomly perturbed 1-D velocity models that the major source of the GF uncertainty is related to random time shifts of the GFs. This allows us to derive closed-form formulae for approximate auto- and cross-covariance functions to simplify the evaluation of the GF uncertainty avoiding any demanding computations. The proposed approximate covariances are tested on examples of moment tensor inversions using both synthetic and real data sets.

2 COVARIANCE OF GREEN FUNCTIONS

In the Bayesian framework, the uncertainty of source inversions relies on statistical description of the GF uncertainty. In accordance with other authors, we assume that it can be described by a correlated multivariate Gaussian PDF characterized by a covariance matrix. To understand the relation between the uncertainty of the GFs and imprecise knowledge of the velocity model, we analyse the dependence of the covariance on velocity model perturbations using Monte-Carlo simulations considering stations at various distances and data in various frequency ranges. Then we propose methodologies for approximate yet simple estimation of the GF covariances.

2.1 Monte-Carlo estimation

We treat a GF due to randomly perturbed velocity model as random function $x(t)$. The cross-covariance function (XCF) $x\text{cov}$ of two random GFs $x(t)$ and $y(t)$ is defined as

$$x\text{cov}(t, \tau) \stackrel{\text{def}}{=} E\{x(t)y(t + \tau)\} - E\{x(t)\}E\{y(t + \tau)\}, \quad (1)$$

where $E\{\dots\}$ denotes expectation (mean over realizations of $x(t)$ and $y(t)$), t is time and τ is a time lag between samples (e.g. Marple 1986). Auto-covariance function (CF) can be derived from eq. (1) considering $y(t) = x(t)$,

$$\text{cov}(t, \tau) \stackrel{\text{def}}{=} E\{x(t)x(t + \tau)\} - E\{x(t)\}E\{x(t + \tau)\}. \quad (2)$$

A straightforward, though computationally demanding, approach to evaluate the covariances is by Monte-Carlo simulations (e.g. Tarantola 2005, pp. 41–55), where the expectations in eqs (1) and (2) are directly obtained from a set of possible GFs for a particular source–receiver settings. For this purpose, we consider an initial velocity model and its 1500 random variations (Fig. 1a). In particular, following Tarantola (2005, pp. 164–170), we randomly vary logarithms of incompressibility modulus κ^* , shear modulus μ^* , and layer thicknesses. The parameters are changed independently to each other and also independently in all layers, assuming Gaussian distribution characterized by standard deviation σ_M expressed in percentage of the initial (mean) value.

We simulate GFs for source–receiver distances 10, 50 and 100 km in the random realizations of the velocity models by discrete wavenumber method (Bouchon 1981), assuming a Dirac delta function as the source time function. GFs computed in the mean velocity model are referred to as the ‘mother’ GFs. Fig. 1(b) shows examples of the generated GFs. They are similar in shape even though the velocity model perturbations are as large as 10 per cent in the present example (maximal correlation coefficients are higher than 0.7 for all the generated GFs). A pronounced effect of the velocity model variations is represented by shifts of the generated waveforms in time. These time shifts (evaluated in this synthetic test from low-frequency waveforms to avoid cycle skipping) have approximately Gaussian distribution with standard deviation σ_t as demonstrated by the histogram in Fig. 1(c). As illustrated in Fig. 1(d), the characteristic width L of the time shift distribution defined as $L = 4\sigma_t$ increases approximately linearly with the velocity model perturbations σ_M with rate depending on the epicentral distance.

Solid lines in Figs 2(a) and (b) show examples of the CFs of a single GF component determined from the set of simulated GFs using eq. (2) for various lags τ and strengths of the velocity model perturbations σ_M . The CFs for given lag τ between samples of the GFs are clearly non-stationary, that is, depending, generally, on time (see Figs 2a and b). The CFs determined this way could be used, in principle, for construction of the full covariance matrix (shown in Fig. 2c). However, the Monte-Carlo technique is very demanding on computational power.

2.2 Approximate covariance function

Here we propose to substitute the demanding Monte-Carlo estimation of the GF covariance by a simplified approach, assuming that the only effect of the velocity model perturbations on the covariances is the time shift of the mother GFs. As we demonstrate later in Section 2.4, despite of this rather strong assumption, the approximate covariances reproduce variations of both the arrival time and the waveform amplitudes.

Let us point out that the proposed methodology is intended to deal with unknown velocity model perturbations that are close to the mean model. In particular, it is not meant to substitute (or correct for) missing velocity structures with strong effects on the waveforms, such as deep sedimentary basins. If some stations are affected by such structures, the modelling should either account for them or such stations should be omitted from the inversion. In

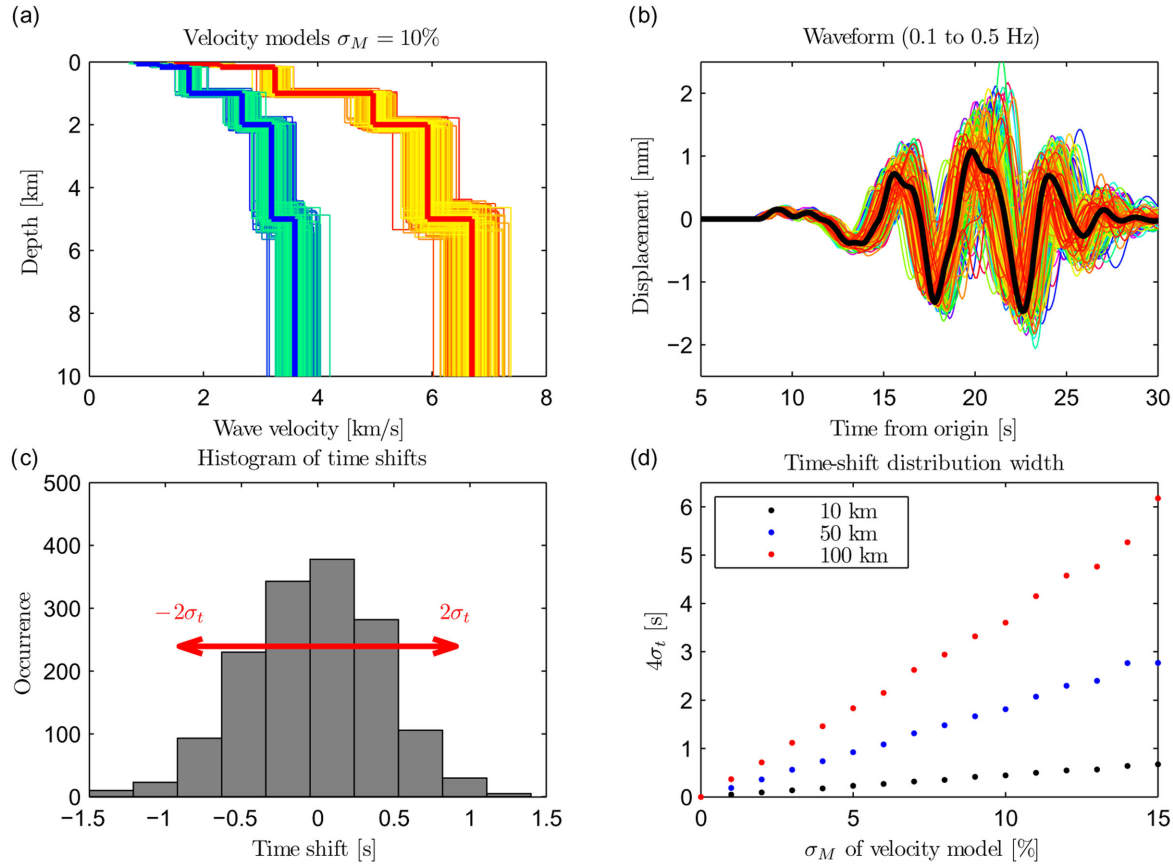


Figure 1. Monte-Carlo simulations. (a) Example of the set of randomly perturbed velocity models with standard deviation $\sigma_M = 10$ per cent. The red/blue lines are the mean P -/S-wave velocity profiles and warm/cold colours are the P -/S-wave velocities of the perturbed models, respectively. (b) Examples of the GFs at one component simulated by the discrete wavenumber method for the source–receiver distance of 50 km ($\sigma_M = 10$ per cent). The black line is the ‘mother’ GF calculated in the mean velocity model. Other colours of waveforms have no meaning and are used only for clearer view. (c) Distribution of time shifts of GFs from panel b estimated from waveforms filtered at very low frequencies (0.05–0.09 Hz) to avoid cycle skipping. The red line shows its characteristic width $4\sigma_t$. (d) The dependence of the characteristic width of the time shift distribution ($4\sigma_t$) on the strength of the velocity model perturbations σ_M for three source–receiver distances (see legend).

any case, we point out that any (even 3-D) velocity model is subject to uncertainty, which could be accounted for by our simplified approach.

Let us derive the approximate formulae for XCF of two, generally different, waveforms with random time shifts. We consider two ‘mother’ waveforms $f(t)$ and $g(t)$ representing GFs in the mean velocity model. Assuming that these waveforms are randomly shifted in time, we define new (random) waveforms $x(t) = f(t - l_1)$ and $y(t) = g(t - l_1 - l_{12})$. Time shift l_1 is random but the same for both signals, while l_{12} characterizes their relative random time shift. We denote PDFs of l_1 and l_{12} as $p_1(l_1)$ and $p_{12}(l_{12})$, respectively. Expectations $E\{\dots\}$ in eq. (1) can be evaluated using mother waveforms and the PDFs $p_1(l_1)$ and $p_{12}(l_{12})$ as

$$E\{x(t)\} = \int_{-\infty}^{\infty} f(t - l_1) p_1(l_1) dl_1 \quad (3)$$

$$E\{y(t + \tau)\} = \int_{-\infty}^{\infty} \int_{-\infty}^{\infty} g(t + \tau - l_1 - l_{12}) p_{12}(l_{12}) p_1(l_1) dl_{12} dl_1 \quad (4)$$

$$\begin{aligned} E\{x(t)y(t + \tau)\} &= \int_{-\infty}^{\infty} \int_{-\infty}^{\infty} f(t - l_1) g(t + \tau - l_1 - l_{12}) \\ &\quad \times p_{12}(l_{12}) p_1(l_1) dl_{12} dl_1. \end{aligned} \quad (5)$$

The XCF formula for general PDFs, $p_1(l_1)$ and $p_{12}(l_{12})$ can be obtained by putting eqs (3)–(5) into eq. (1), requiring only specification of the mother waveforms and PDFs of the time shifts. It is, in principle, applicable in covariance matrix estimation; nevertheless, the formula can be further simplified by assuming that the time shifts are uniformly distributed,

$$p_1(l_1) = \Pi_{L_1}(l_1), \quad (6)$$

$$p_{12}(l_{12}) = \Pi_{L_{12}}(l_{12}), \quad (7)$$

where Π_L is a boxcar function of unit area centred around zero with duration L . The expectations of the random processes in eqs (3)–(5) then simplify to

$$E\{x(t)\} = \frac{1}{L_1} \int_{-\frac{L_1}{2}}^{\frac{L_1}{2}} f(t - l_1) dl_1 \quad (8)$$

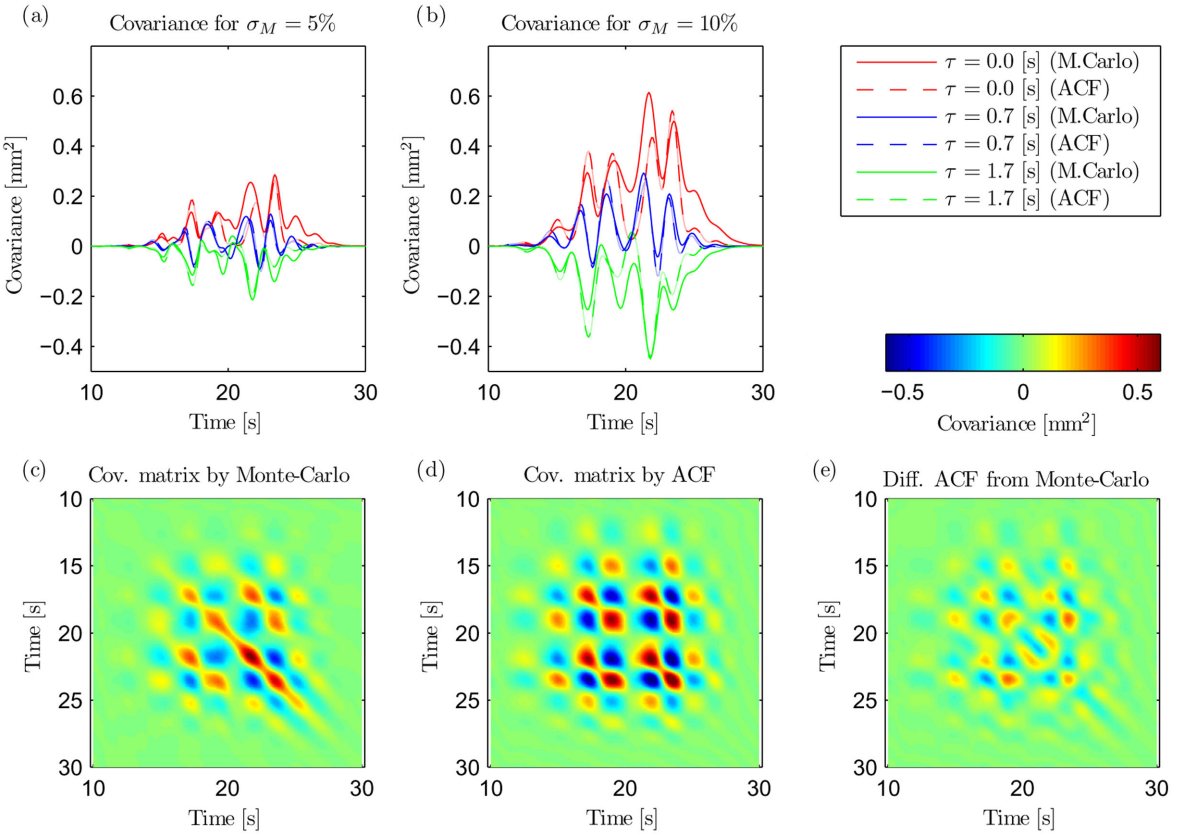


Figure 2. Examples of the GF covariances. Panels (a) and (b) show time dependence of the covariances assuming velocity model perturbations of strengths $\sigma_M = 5$ per cent and $\sigma_M = 10$ per cent, respectively, for three selected time lags (see legend) estimated using the Monte-Carlo simulations (solid lines) and approximate formula (12) (dashed lines). The GFs are calculated for source-receiver distance 50 km and are filtered between 0.1–0.5 Hz. The width of the uniform PDF $L_1 = 4\sigma_t$ used in the approximate formula is adopted from the graph in Fig. 1(d). Panels (c) and (d) show full covariance matrices estimated by Monte-Carlo simulations and using formula (12), respectively, assuming velocity model perturbations with $\sigma_M = 10$ per cent. Panel (e) displays the differences between the latter two covariance matrices.

$$\begin{aligned} E \{y(t + \tau)\} &= \frac{1}{L_1} \int_{-\frac{L_1}{2}}^{\frac{L_1}{2}} \frac{1}{L_{12}} \int_{-\frac{L_{12}}{2}}^{\frac{L_{12}}{2}} \\ &\times g(t + \tau - l_1 - l_{12}) dl_{12} dl_1 \end{aligned} \quad (9)$$

$$\begin{aligned} E \{x(t)y(t + \tau)\} &= \frac{1}{L_1} \int_{-\frac{L_1}{2}}^{\frac{L_1}{2}} \frac{1}{L_{12}} \int_{-\frac{L_{12}}{2}}^{\frac{L_{12}}{2}} f(t - l_1) \\ &\times g(t + \tau - l_1 - l_{12}) dl_{12} dl_1. \end{aligned} \quad (10)$$

Putting eqs (8)–(10) into eq. (1), the final formula for approximate cross-covariance (ACF) $x\tilde{cov}$ reads:

$$\begin{aligned} x\tilde{cov}(t, \tau) &= \frac{1}{L_1 L_{12}} \int_{-\frac{L_1}{2}}^{\frac{L_1}{2}} \int_{-\frac{L_{12}}{2}}^{\frac{L_{12}}{2}} \\ &\times f(t - l_1) g(t + \tau - l_1 - l_{12}) dl_{12} dl_1 \\ &- \frac{1}{L_1} \int_{-\frac{L_1}{2}}^{\frac{L_1}{2}} f(t - l_1) dl_1 \quad \frac{1}{L_1 L_{12}} \int_{-\frac{L_1}{2}}^{\frac{L_1}{2}} \int_{-\frac{L_{12}}{2}}^{\frac{L_{12}}{2}} \\ &\times g(t + \tau - l_1 - l_{12}) dl_{12} dl_1. \end{aligned} \quad (11)$$

Approximate auto-covariance (ACF) can be derived analogously from eq. (2), or from eq. (11) considering that the mother waveforms

are identical, $g(t) = f(t)$, and that PDF $p_{12}(l_{12})$ becomes formally a Dirac delta function. The final formula for ACF (\tilde{cov}) then reads:

$$\begin{aligned} \tilde{cov}(t, \tau) &= \frac{1}{L_1} \int_{-\frac{L_1}{2}}^{\frac{L_1}{2}} f(t - l_1) f(t + \tau - l_1) dl_1 \\ &- \frac{1}{L_1} \int_{-\frac{L_1}{2}}^{\frac{L_1}{2}} f(t - l_1) dl_1 \quad \frac{1}{L_1} \int_{-\frac{L_1}{2}}^{\frac{L_1}{2}} f(t + \tau - l_1) dl_1. \end{aligned} \quad (12)$$

The ACF formula thus requires only specification of the mother waveform (i.e. GF in the mean velocity model) and the width of the uniform time shift distribution L_1 . Eq. (12) is easy to implement as the integrals normalized by $1/L_1$ operate as smoothing by a moving time window of width L_1 .

To illustrate the performance of the proposed simplified formulae, we use ‘mother’ GFs from the above-described Monte-Carlo simulations and consider uniform $p_1(l_1)$ with width $L_1 = 4\sigma_t$, where σ_t is estimated from the Monte-Carlo simulations (see Fig. 1c). The resulting ACFs for such setting are shown in Figs 2(a) and (b) by dashed lines. They fit very well the main features of the CFs from the Monte-Carlo simulations (solid lines), confirming that in terms of the CFs the time shifts are indeed the dominant effect of the velocity model uncertainty. We note that this approximate approach is very effective because it skips the very demanding computation of thousands of GFs in the Monte-Carlo approach. A set of ACFs

for different time lags then compose the full covariance matrix (Fig. 2d), which is again close to the full covariance matrix from the Monte-Carlo simulations (Fig. 2c) in terms of its pattern including signs. The rather minor differences between the two covariance matrices are shown in Fig. 2(e) and discussed in more detail in Section 2.4.

2.3 Stationarized covariance function

Here we introduce even stronger simplification of the covariance function. The motivation is as follows. Since the real elastic parameters of the Earth are rather complex (3-D, anisotropic, etc.), the covariance determined by Monte-Carlo simulations might not reflect the reality perfectly. Nevertheless, we can assume that the overall pattern of the simulated CFs and ACFs effectively captures the main features of the GFs uncertainty. In particular, we consider that such representative of the true uncertainty for each time lag τ is just the CF's average over time, $\frac{1}{T} \int_{-\infty}^{\infty} \text{cov}(t, \tau) dt$, where T is duration of the dominant part of the signal. By calculating the mean of the (non-stationary) CF over time we obtain covariance dependent only on the time lag, which is property of so-called wide-sense stationary random signals (e.g. Marple 1986), and thus we denote this approach as stationarization. For example, when the stationarized covariance function (SCF) is evaluated from the ACF, we call it stationarized approximate covariance function (SACF),

$$\overline{\text{cov}}(\tau) \stackrel{\text{def}}{=} \frac{1}{T} \int_{-\infty}^{\infty} \widetilde{\text{cov}}(t, \tau) dt. \quad (13)$$

Note that this simplification will also help us to better understand the role of the covariance function in the source inversion (see Section 3.4). Since the SACFs are by definition stationary (i.e. depending only on lag τ), the respective covariance matrix has Toeplitz structure (diagonal-constant). Such property may be useful in specific (e.g. large-scale or iterative) applications because it permits very cheap calculation of the matrix's inverse, which is required when solving inverse problems (e.g. Tarantola 2005, pp. 62–68; Trench 1964). Note that the stationarized approximate cross-covariance (SAXCF) $\overline{x\text{cov}}(\tau)$ can be defined analogously, substituting $\widetilde{\text{cov}}$ by $\widetilde{x\text{cov}}$ in eq. (13).

Considering GFs with random time shifts with uniform distribution, one can derive closed-form formulae for the SACFs and SAXCFs as follows (for detailed derivation, see the Supporting Information):

$$\overline{\text{cov}}(\tau) = \frac{1}{T} [r_f(\tau) - \wedge_{2L_1}(\tau) * r_f(\tau)], \quad (14)$$

$$\overline{x\text{cov}}(\tau) = \frac{1}{T} \Pi_{L_{12}}(\tau) * [r_{fg}(\tau) - \wedge_{2L_1}(\tau) * r_{fg}(\tau)]. \quad (15)$$

Here star represents convolution, $\wedge_{2L_1}(\tau)$ is the triangle function of unit area centred around zero with duration $2L_1$, and $r_f(\tau) \stackrel{\text{def}}{=} \int_{-\infty}^{\infty} f(t)f(t+\tau) dt$, and $r_{fg}(\tau) \stackrel{\text{def}}{=} \int_{-\infty}^{\infty} f(t)g(t+\tau) dt$ are auto- and cross-correlations of the ‘mother’ GFs, respectively. $\Pi_{L_{12}}(\tau)$ is the time-centred boxcar function with base equal to L_{12} and with unit area.

Figs 3(a) and (b) show examples of the SACFs (red lines) obtained using eq. (14). We consider the width of the uniform PDF L_1 equal to the characteristic width of the time shift distributions from the Monte-Carlo simulations (Fig. 1d), $L_1 = 4\sigma_t$. In Figs 3(a) and (b), we scale the covariances by the arithmetic mean of the squares of the signal f (i.e. square of the signal root-mean-square, $\text{RMS}^2(f(t))$)

as it represents the maximum possible value of $\overline{\text{cov}}$. Indeed, by definition, the auto-correlation r_f has its maximum value at the zero time lag, and from eq. (14) it follows

$$\lim_{L_1 \rightarrow \infty} (\overline{\text{cov}}(0)) = \frac{r_f(0)}{T} = \text{RMS}^2(f(t)). \quad (16)$$

Note that RMS^2 (i.e. ‘signal energy density’) is determined from the dominant part of the earthquake signal defined by the interval T .

Fig. 3 compares the SACFs (in red) with the SCFs estimated by the Monte-Carlo approach (in black). The agreement is very good even for velocity model perturbations as large as 15 per cent in the present example despite all the simplifications made. Let us point out that, interestingly, the shape of the stationarized CFs is similar to those obtained ‘empirically’ from waveform residuals by Dettmer *et al.* (2007, 2014), suggesting that their posterior estimate of the data uncertainty is dominated by the velocity model uncertainty.

Let us discuss here specifically the zero time lag of the CF, expressing variance (uncertainty) of the GF at each time sample t (Figs 2a and b, in red lines). In particular, after stationarization of the CF (Figs 3a and b, zero time lag), where the zero time lag represents mean GF variance over the waveform duration. We evaluate the dependence of the SCFs' zero time lag on various parameters: source–receiver distances, Butterworth filtering frequencies, and strengths of velocity model perturbations σ_M . Fig. 4 shows these dependences obtained by the approximate approach (dashed lines) as compared with the those obtained from the Monte-Carlo simulations (solid lines). The variances for absolutely correct velocity model ($\sigma_M = 0$) are equal to zero by definition as there is no possible variation of GFs. The variances then asymptotically increase with increasing velocity model uncertainty up to the case of variations as large as the RMS^2 . The increase of the GF variations is steeper for larger source–receiver distances (i.e. as the wave travel-time through the inaccurate velocity model increases), and also for higher considered frequencies (i.e. as the number of wavelengths along the path increases).

We can relate our estimate of the GFs variance to an independent finding of Gallovič & Ampuero (2015), who compared results of synthetic slip inversion benchmark test SIV2a (Mai *et al.* 2016) as obtained by several modellers. They concluded that the results were consistent up to approximately 1/10 of the maximum singular value of the forward design matrix, which corresponds to less than 1 per cent mean data error ($\overline{\text{cov}}/\text{RMS}^2 = 0.01$). Since very close stations and low-frequency data were considered in the benchmark, Fig. 4(a) suggests that modellers had imprecise GF in terms of velocity model perturbations $\sigma_M \lesssim 2$ per cent. Such velocity model uncertainty can be translated using Fig. 1(d) to very small error of arrival times $\sigma_t \lesssim 0.02[s]$, which can be related just to some minor inconsistencies among the modeller setups (including possible small shifts of the considered fault plane).

2.4 Performance of the approximated covariances in capturing the GF variations

Covariance matrices and their approximations are used to statistically describe the uncertainty of the GFs. However, it is not trivial to assess the quality of the proposed approximations in terms of capturing the true variability of the GFs. In other words, it is not evident what kind of GF variability is actually captured by the

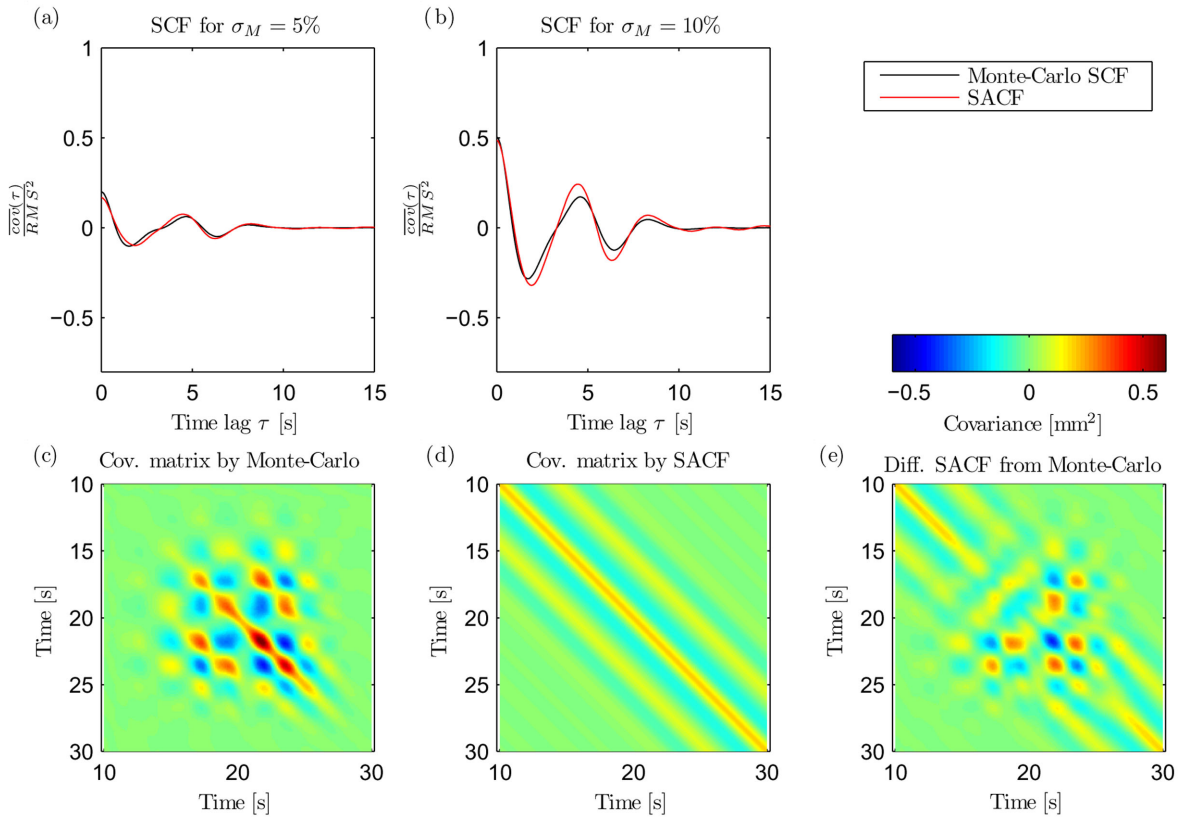


Figure 3. Examples of the stationarized auto-covariances (SCFs). Panels (a) and (b) show the SCF for two strengths of the model perturbations, $\sigma_M = 5$ per cent and $\sigma_M = 10$ per cent, respectively, obtained by the Monte-Carlo simulations (black lines) and by the approximate formula eq. (14) (SACF, red lines). The source-receiver distance is 50 km and the GFs are filtered in range 0.1–0.5 Hz. The width of the uniform PDF $L_1 = 4\sigma_t$ used in the approximate formula is adopted from the graph in Fig. 1(d). Duration of the dominant part of the earthquake signal $T = 15$ sec. The SCF values on y-axis are scaled by the signal energy density, that is, the mean square amplitude of the signal (RMS^2). Panels (c) and (d) show full covariance matrices for velocity model perturbations corresponding to $\sigma_M = 10$ per cent as obtained by the non-stationarized Monte-Carlo approach and using SACF formula in eq. (14), respectively. Panel (e) shows the difference between the SACF and the Monte-Carlo non-stationarized covariance matrices.

approximated covariances. To address this issue, we draw random GF samples from their multivariate normal distributions described by the mother waveforms and the covariance matrices to visually inspect their effects on the GF variability. Examples of random GFs generated considering the various covariance matrices introduced herein are shown in Fig. 5. For drawing the random samples, we use Matlab function *mvnrnd*.

Random GFs generated using the ‘Monte-Carlo’ covariance matrix (Fig. 5b) may serve as a reference set. They reasonable agree with the variability of the original set of the GFs calculated for the randomly perturbed velocity models (see Fig. 1b). Spread of the GFs generated by the ACF matrix (Fig. 5d) is very similar to the reference (Fig. 5b), especially when taking into account the great difference in the computational demands. Indeed, the random GFs generated using the ACF matrix have similar time shifts and zero values prior and after the useful signal as the reference GFs. We note that the variations in GF amplitudes might come as a surprise because the ACF formula in eq. (12) was derived assuming pure time shifts without any change of the signal shape. This is due to the fact that the Gaussian PDF is not, strictly speaking, a good statistical model for capturing such variations. In other words, the variations in amplitudes represent an artefact of using an inappropriate statistical model for the randomly shifted signal in a mathematical sense. Nevertheless, despite being an artefact, we consider it advantageous for our purpose since the ACF then captures more general variabil-

ity that is closer to the reference one obtained by the expensive Monte-Carlo approach.

Variability of GFs for the SACF matrix (Fig. 5f) is similar to the reference only in the time interval where the ‘mother’ GF has the strongest signal (i.e. from 15 to 26 s). Outside of this time interval, the time-independence of the SACF leads to generation of strong amplitude variations unobserved in the reference set. If needed, these variations could be suppressed by applying an additional taper on the rows and columns of the respective covariance matrix (see Fig. 3e), reducing values in their upper-left and bottom-right corners.

For illustration purposes, we show in Fig. 5(h) also the case of a diagonal covariance matrix since it is most typically considered in practical source inversions. The resulting random samples of the GFs correspond to the mother waveform perturbed by a white (uncorrelated) Gaussian noise in the whole time window.

3 EXAMPLE OF APPLICATION OF THE APPROXIMATE COVARIANCES IN MOMENT TENSOR INVERSION

The proposed approximate covariances can be easily implemented into existing seismic source inversions based on waveform modelling including those formulated in the Bayesian framework. For example, it can be used in source inversion proposed by, for

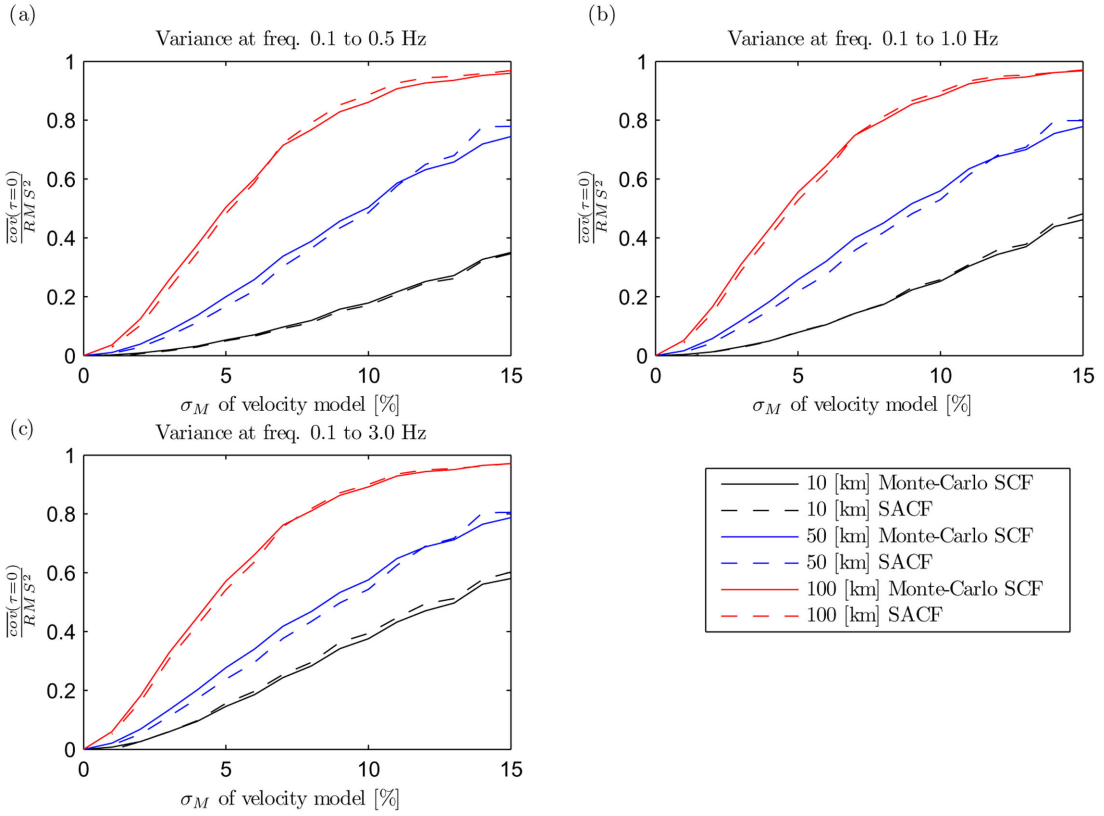


Figure 4. The dependence of the GF variance (SCFs at zero time lags) on various parameters estimated by the Monte-Carlo simulations (solid lines) and using the approximate formula for SACFs (dashed lines). The individual panels correspond to GFs filtered in various frequency ranges: (a) 0.1–0.5 Hz, (b) 0.1–1.0 Hz and (c) 0.1–3.0 Hz. In each panel, colours distinguish the source-receiver distance (see legend), the strength of the velocity model perturbations is on the x-axis and the variance scaled by RMS^2 of the mother waveform (representing maximum possible value of the variance) is on the y-axis.

example, Yagi & Fukahata (2011) or Duputel *et al.* (2012), where the covariance matrix of the modelling errors (describing the GFs uncertainty) is added to the data covariance matrix describing the seismic noise. In those approaches, the covariance of the modelling error is iteratively updated every source model update. Here we show an alternative, simplified, Bayesian approach, assuming that the data error is mainly due to the velocity model uncertainty. In other words, the modelling error covariance is estimated using the approximate formulae in eqs (12) and (14) evaluated directly from the observed waveforms. This allows us to solve the inverse problem very efficiently without any iterations.

For the present example of moment tensor (MT) inversion we consider a near-regional distribution of broad-band stations in the Corinth Gulf, Greece (Fig. 6). Besides a synthetic example, for which the target waveforms are generated in velocity models randomly perturbed for each station, we show also a real-data inversion in the same setting.

3.1 Inversion method

We follow the approach of Kikuchi & Kanamori (1991), where the full seismic MT is parameterized by six elementary MTs ($\mathbf{M}_1 \dots \mathbf{M}_6$) defined therein. Full MT is then composed of their linear combination described by six coefficients ($a_1 \dots a_6$),

$$\mathbf{M} = \sum_{n=1}^6 a_n \mathbf{M}_n = \begin{pmatrix} a_2 - a_5 + a_6 & a_1 & a_4 \\ a_1 & -a_2 + a_6 & a_3 \\ a_4 & a_3 & a_5 + a_6 \end{pmatrix}. \quad (17)$$

For each of the elementary MT n , we evaluate elementary seismogram \mathbf{E}_r^n by the discrete wavenumber method for a receiver r (vectors \mathbf{E} consists of temporal samples). Synthetic seismogram \mathbf{u}_r for a general MT in eq. (17) can then be obtained by a linear combination of the six elementary seismograms,

$$\mathbf{u}_r = \sum_{n=1}^6 a_n \mathbf{E}_r^n = \mathbf{G}\mathbf{m}, \quad (18)$$

where $\mathbf{m} = (a_1, a_2, a_3, a_4, a_5, a_6)^T$ and \mathbf{G} is linear operator of the forward problem consisting of the elementary seismograms \mathbf{E}_r^n . Generalization to more stations and components is straightforward.

The advantage of such linear formulation is the possibility to pre-compute the elementary seismograms for all receivers, and then easily find coefficients including their errors by means of the Bayesian approach (Tarantola 2005, pp. 62–68). Indeed, assuming that observed data \mathbf{d}_{obs} are characterized by Gaussian data errors with covariance matrix \mathbf{C} and considering no prior information, the posterior PDF reads

$$\text{pdf}(\mathbf{m} | \mathbf{d}_{\text{obs}}) = \text{const. } \exp \left(-\frac{1}{2} (\mathbf{d}_{\text{obs}} - \mathbf{G}\mathbf{m})^T \mathbf{C}^{-1} (\mathbf{d}_{\text{obs}} - \mathbf{G}\mathbf{m}) \right), \quad (19)$$

where ‘const.’ is a normalization constant. This Gaussian function attains its maximum for

$$\tilde{\mathbf{m}} = (\mathbf{G}^T \mathbf{C}^{-1} \mathbf{G})^{-1} (\mathbf{G}^T \mathbf{C}^{-1} \mathbf{d}_{\text{obs}}), \quad (20)$$

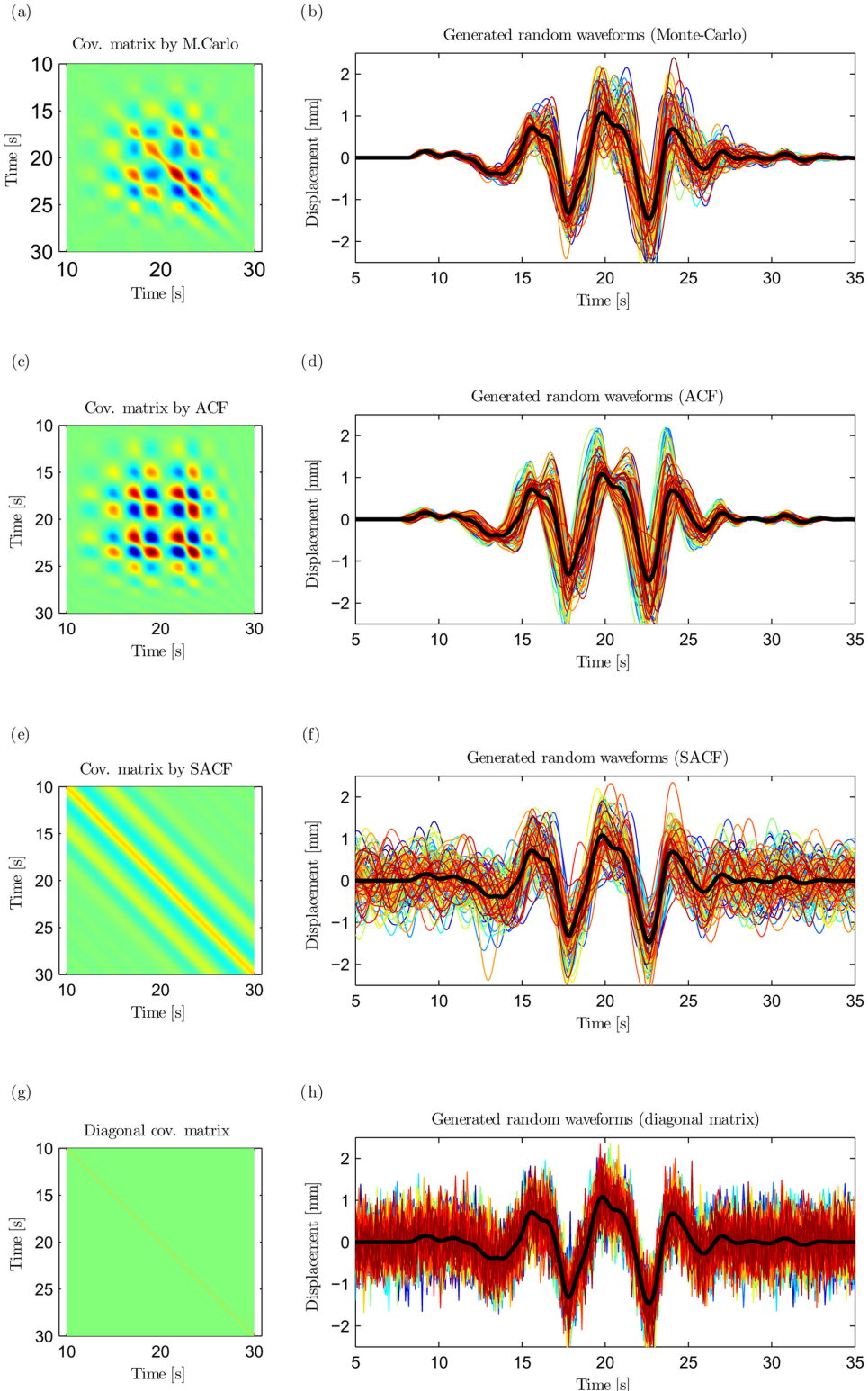


Figure 5. Examples of GFs (b, d, f, h) generated as random samples from multivariate Gaussian distributions described by a ‘mother’ GFs (in bold black) and the various covariance matrices shown in the respective panels (a, c, e, g), see legend. The colour scale used for the covariance matrices is the same as in Figs 2 and 3. Waveform colours have no meaning and are used just for clearer view. The source–receiver distance for this example is 50 km, and the strength of the model perturbation $\sigma_M = 10$ per cent.

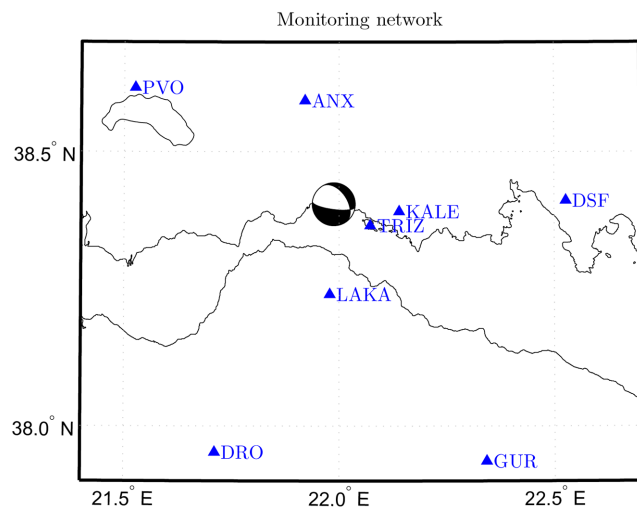


Figure 6. Seismic station distribution (triangles) in the Corinth Gulf used in the MT inversion tests. The beachball plotted at the event epicentre corresponds to the mechanism considered in the synthetic test (after Sokos & Zahradník 2013).

which is called best-fitting or maximum likelihood solution. The shape of the Gaussian PDF is characterized by the (posterior) covariance matrix $\tilde{\mathbf{C}}$ given by

$$\tilde{\mathbf{C}} = (\mathbf{G}^T \mathbf{C}^{-1} \mathbf{G})^{-1}. \quad (21)$$

The 6×6 elements of matrix $\tilde{\mathbf{C}}$ fully describe the uncertainty of the inverted MT solution.

Let us explain an alternative view of the role of the data covariance matrix in the Bayesian inversion. Covariance matrix is by definition positive semi-definite, and if it is, moreover, positive definite, its inverse exists and can be factorized by Cholesky decomposition,

$$\mathbf{C}^{-1} = \mathbf{R}^T \mathbf{R}, \quad (22)$$

where \mathbf{R} is an upper triangular matrix. Putting eq. (22) into eq. (19), the posterior PDF can be rewritten as

$$\text{pdf}(\mathbf{m} | \mathbf{d}_{\text{obs}}) = \text{const. } \exp \left(-\frac{1}{2} (\mathbf{R} \mathbf{d}_{\text{obs}} - \mathbf{R} \mathbf{G} \mathbf{m})^T (\mathbf{R} \mathbf{d}_{\text{obs}} - \mathbf{R} \mathbf{G} \mathbf{m}) \right), \quad (23)$$

meaning that the best-fitting solution minimizes L2 norm of so-called standardized residuals obtained as a difference between the data and synthetics after they both are multiplied by the triangular matrix \mathbf{R} from the Cholesky decomposition.

3.2 Source inversion of synthetic data set

We assume an earthquake from the Corinth Gulf, Greece, at depth 8 km and with moment magnitude 5.4. Fig. 6 shows the source location and the station geometry. Synthetic data for the inversion test were computed by the discrete wavenumber method (Bouchon 1981) assuming a Dirac delta function as the source time function and pure shear mechanism with strike 327° , dip 32° , and rake -45° . The waveforms were filtered by Butterworth bandpass filter with corner frequencies 0.1 to 0.2 Hz and then downsampled to 5 Hz sampling rate. In the following tests, we generate ‘data’ for the inversion assuming a realization of random variations of the wave speeds and depths of the layers (as in the Monte-Carlo simulations described in Section 2.1) for each station independently ($\sigma_M = 10$ per cent). Such random variations of the reference velocity model

simulate a real case when the velocity model is complex, yet well described by a mean velocity model. In all tests, the inversions are performed in the reference (mean) layered velocity model.

3.2.1 Covariance matrices describing the velocity model uncertainty

In multistation and multi-component inversion the data covariance matrix has a block structure. Auto-covariance matrices for the individual waveforms are arranged along the diagonal, while off-diagonal blocks contain cross-covariance matrices among the individual waveforms. Here we describe six covariance matrices that are tested in the following inversions.

The simplest case when the crustal model uncertainty is disregarded in the inversion is represented by a diagonal covariance matrix with constant variance equal to the square of 1/50 of the maximum signal amplitude from the entire data set (i.e. relatively weak noise corresponding to the almost negligible ambient noise in the real-data inversion in Section 3.3). We also consider a diagonal covariance matrix consisting of diagonal values from the SACF, which implicitly weights the waveforms considered. Furthermore, we consider covariance matrices with off-diagonal components obtained using ACF and SACF. We apply an additional taper on the rows and columns of the SACF matrix (see Fig. 3e) as suggested in Section 2.4. Finally, we show the case when even approximate cross-covariances between components of the same receiver are taken into account using the AXCF and (tapered) SAXCF. Note that we add the constant weak-noise variance discussed above to all the covariance matrices considered to ensure positive definiteness of the covariance matrix.

Formulae for the approximate covariances require definition of the width of the uniform PDF describing the time-shift distribution, L_1 . We consider a linear dependence on source-receiver distance, following values for $\sigma_M = 10$ per cent in graph Fig. 1(d). The implemented dependence reads

$$L_1 [s] = \begin{cases} 1.5 & \text{for } \frac{d}{25} \leq 1.5 \\ \frac{d}{25} & \text{for } \frac{d}{25} > 1.5 \end{cases} \quad (24)$$

where d is a source-receiver distance in kilometres. Example of sub-matrices of the six covariance matrices corresponding to a selected station can be found in the Supporting Information.

3.2.2 Properties of the maximum likelihood solution

The MT inversion is performed for 1000 different target data sets computed in randomly perturbed velocity models. For each realization, we obtain best-fitting solutions for each type of the covariance matrix considered. Fig. 7 shows the ensemble of the solutions displayed in terms of DC mechanism nodal planes, and histograms of maximum difference to the true model in strike, dip, rake, DC component ratio and the inferred scalar seismic moment M_0 . We note that the spread of the differences to the reference solution (plotted in red) is caused by variations of the randomly perturbed velocity model, hence by the GFs uncertainty.

The maximum difference in the angles of the DC mechanisms reaches 10° – 20° depending on the covariance matrix type considered. Asymmetry of the DC mechanism angle difference (e.g. Fig. 7d) is related to the particular spatial settings of the monitoring network. The DC component ratios are scattered from the simulated pure shear (DC = 1) down to values 0.8–0.6. The variability

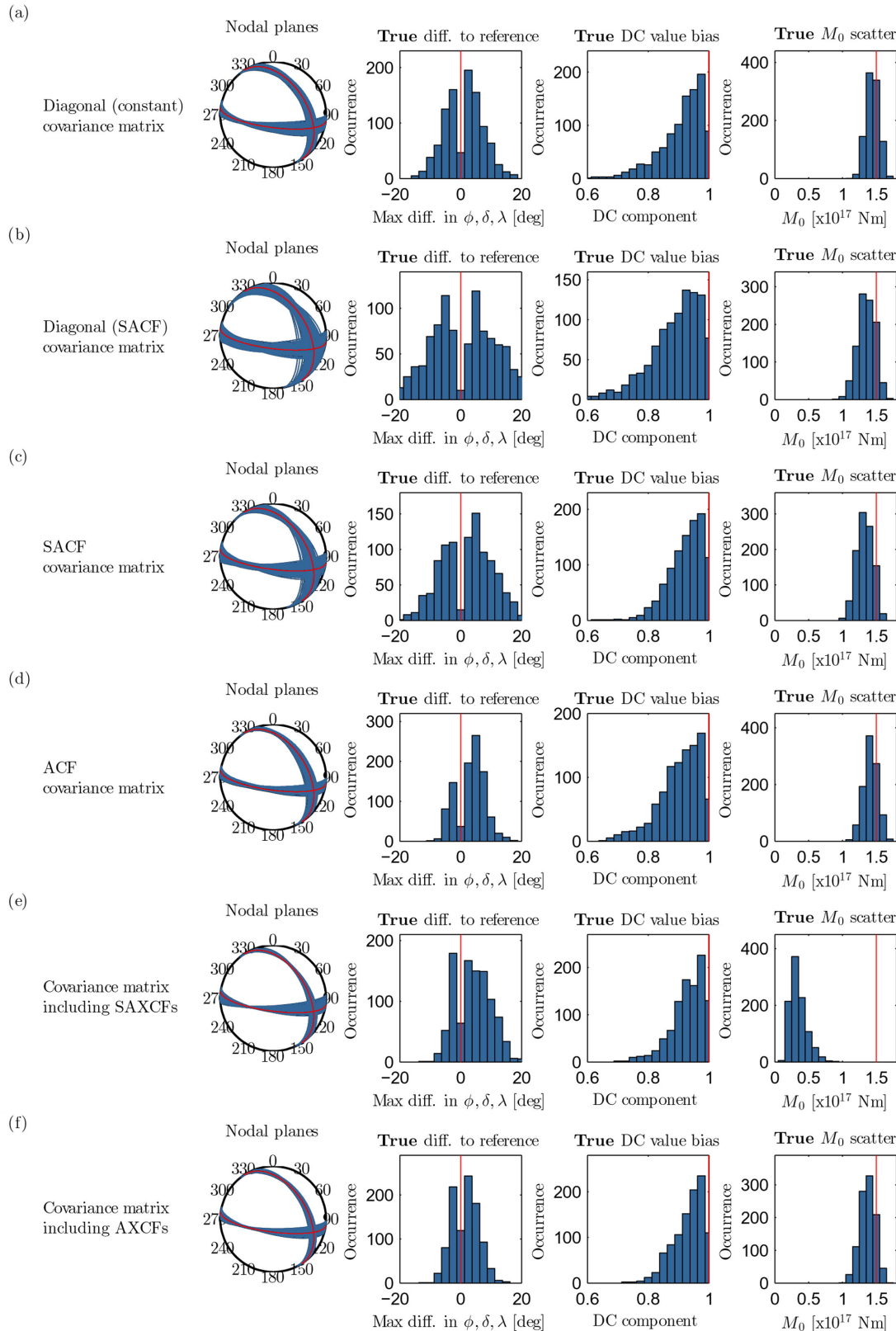


Figure 7. Statistical analysis of best-fitting solutions from MT inversion synthetic tests with 1000 realizations of randomly perturbed velocity models used to generate population of target data for the inversion. Panels in each row show DC mechanism nodal planes (left), maximum differences in strike, dip, rake to the reference (middle-left), DC component bias (middle-right) and M_0 scatter (right). Each row corresponds to the use of different type of the data covariance matrix (see legend). The true reference solution (in red) has a pure shear mechanism (DC = 1) with strike 327° , dip 32° , rake -45° , and scalar seismic moment 1.5×10^{17} Nm.

of the inferred scalar moments is similar for all the considered covariance matrix types ranging from 1.0 to 1.6×10^{17} Nm (i.e. 5.3 to 5.4 in moment magnitude scale), except for the SAXCF case. Indeed, the latter type of the covariance matrix leads to significant underestimation of the scalar seismic moment (Fig. 7e). It is perhaps related to the time averaging procedure in the SAXCF definition. Although the time averaging seems to work well for the autocorrelation components in SACF, calculating temporal mean over cross-covariance components in SAXCF representing relation (correlation or even anti-correlation) between individual samples of two waveforms seems to have negative consequences on the inversion. In particular, although nodal planes solution may be similar to the reference, the scalar seismic moment is underestimated in order to reduce the effect of the time inappropriate temporal averaging of the cross-correlations. Thus if cross-covariances are required, the non-stationary type (AXCF) should be preferred.

We note that the presented statistics of the inverted best-fitting parameters can be understood as the ‘true’ MT uncertainty caused by the velocity model uncertainty. Overall assessment of the performance of the individual covariances in Fig. 7 suggests that implementation of ACF (Fig. 7d) possibly in combination with AXCF (Fig. 7f) provides the lowest uncertainty of the inverted MTs. Nevertheless, even in those cases the MT uncertainty remains significant and thus should not be neglected in practical applications. Therefore, in the next section we assess the ability of the individual types of the covariances to estimate the ‘true’ uncertainty in terms of the posterior covariance matrix.

3.2.3 Moment tensor uncertainty estimate

We arbitrarily selected one of the synthetic target data sets, inferred the best-fitting MT solution and estimated its uncertainty in terms of the posterior covariance matrix (eq. 21). For each type of the data covariance matrix, Fig. 8 shows the maximum likelihood solution together with the posterior uncertainty similarly to Fig. 7. However, here the ensemble of the solutions is obtained by random sampling the posterior PDF (using Matlab function *mvnrnd*). In Fig. 8, the true parameters are plotted by red colour for comparison. We note that the best-fitting solutions are biased due to the particular velocity model perturbations considered in the target data. In the following we concentrate on the uncertainty estimation in comparison with the ‘true’ uncertainty as revealed in Section 3.2.2.

In case of the constant diagonal covariance matrix (Fig. 8a), the posterior PDF is characterized by very narrow uncertainty limits in contrast to the ‘true’ uncertainty (Fig. 7a). Such estimate of the MT uncertainty is clearly unacceptable. Slightly better, yet still underestimated, uncertainty is attained when including the ACF covariance matrix (Fig. 8d in comparison with Fig. 7d). It is perhaps due to the slight overestimation of inter-sample cross-covariances in the ACF, which can be visible in Figs 2(e) and 5(d). Inversion with the SACF in Fig. 8(c) provides the largest MT uncertainty estimate, being comparable with that shown in Fig. 7(c). The larger uncertainty estimate is linked to the time-invariance of the SACF covariance matrix allowing for more general waveform changes as can be seen in Fig. 5(f). Finally, considering also the inter-component cross-covariances in the inversion reduces the posterior PDF uncertainty estimate for both the SAXCF (Fig. 8e) and AXCF (Fig. 8f). To conclude, the most reliable estimate of the uncertainty of the MT parameters is revealed when employing covariance matrix built from the SACFs.

3.3 Moment tensor inversion of real data set

Here, we illustrate the proposed methodology on a MT inversion using data written by a real earthquake in Greece. The test event from 25 April 2012 (10:34 UTC) with moment magnitude 4.3 was located in the Corinth Gulf at depth 8 km. Its centroid MT was well examined by the ISOLA full-waveform inversion software by Sokos & Zahradník (2013). The event was recorded by near-regional stations (i.e. broad-band sensors supplemented by accelerograph at station TRIZ). As a reference MT solution for this event we adopt the result obtained by Sokos & Zahradník (2013) when considering the same data set: strike 327° , dip 32° and rake -45° with 87 per cent of DC component. We point out that jack-knifing results of Sokos & Zahradník (2013) indicated rather large variability of the solutions with the most likely value of DC being larger than 95 per cent.

We perform the MT inversion tests in the reference layered velocity model using only high quality records as identified by Sokos & Zahradník (2013, fig. 3). The setting of the real case test is then consistent with that of the synthetic test (Section 3.2, Fig. 6). The waveforms were filtered by Butterworth bandpass filter between 0.1 and 0.2 Hz and then downsampled to 5 Hz sampling rate. The upper bound of the ambient noise, measured prior the useful signal, was estimated $2.8 \mu\text{m}$ corresponding to 1/50 of the maximum signal amplitude from the entire data set. Square of such ambient noise level was used as variance in the diagonal data covariance matrix to show the case when the crustal model uncertainty is disregarded in the inversion. Then we perform inversion tests employing complete covariance matrices analogously to the synthetic tests performed in Section 3.2. The values of L_1 used in this test were adopted from eq. (24).

The inversion results are summarized in Fig. 9. The figure shows the maximum likelihood solution together with the MT uncertainty estimate by means of posterior covariance matrix (eq. 21) for each data covariance matrix considered. The ensemble of the solutions is obtained as random samples of the posterior PDF (using Matlab function *mvnrnd*). The behaviour of the real-data inversion is analogous to the synthetic-data inversion described in Section 3.2. However, the ‘correct’ source parameters (especially the DC parameter) are unknown in this case. The inversion with constant diagonal covariance matrix (i.e. disregarding crustal model uncertainty; Fig. 9a) provides clearly underestimated MT uncertainty. The ACF (Fig. 9d) provides good estimate in terms of the variance reduction, but the uncertainty is still underestimated as it does not fully cover the reference solution. However, the maximum likelihood solution (note especially DC component value in Fig. 9d) seems to be more reliable than in the case of the constant diagonal covariance matrix (Fig. 9a). Inversion with the SACF (Fig. 9c) provides the largest MT uncertainty estimate. We note that the related spread of the possible solutions is similar to that obtained by jack-knifing by Sokos & Zahradník (2013, fig. 3).

The seismograms and the standardized seismograms for all stations and components used in inversion are shown in the Supporting Information. The variance reductions for the best-fitting parameters expressed in term of standardized residuals are 0.72, 0.63, 0.47, 0.67, 0.12 and 0.53 in inversions with diagonal, diagonal SACF, SACF, ACF, SAXCF and AXCF covariance matrices, respectively. The RMS difference between the data and the best-fitting synthetics are 6.91, 7.57, 8.15, 7.36, 11.86 and $7.45 \mu\text{m}$, respectively. Lower value of variance reduction in the inversion with the SACF covariance matrix reflects more complicated shape of the standardized data as shown in Section 3.4 (see Figs 10e and f). The significantly

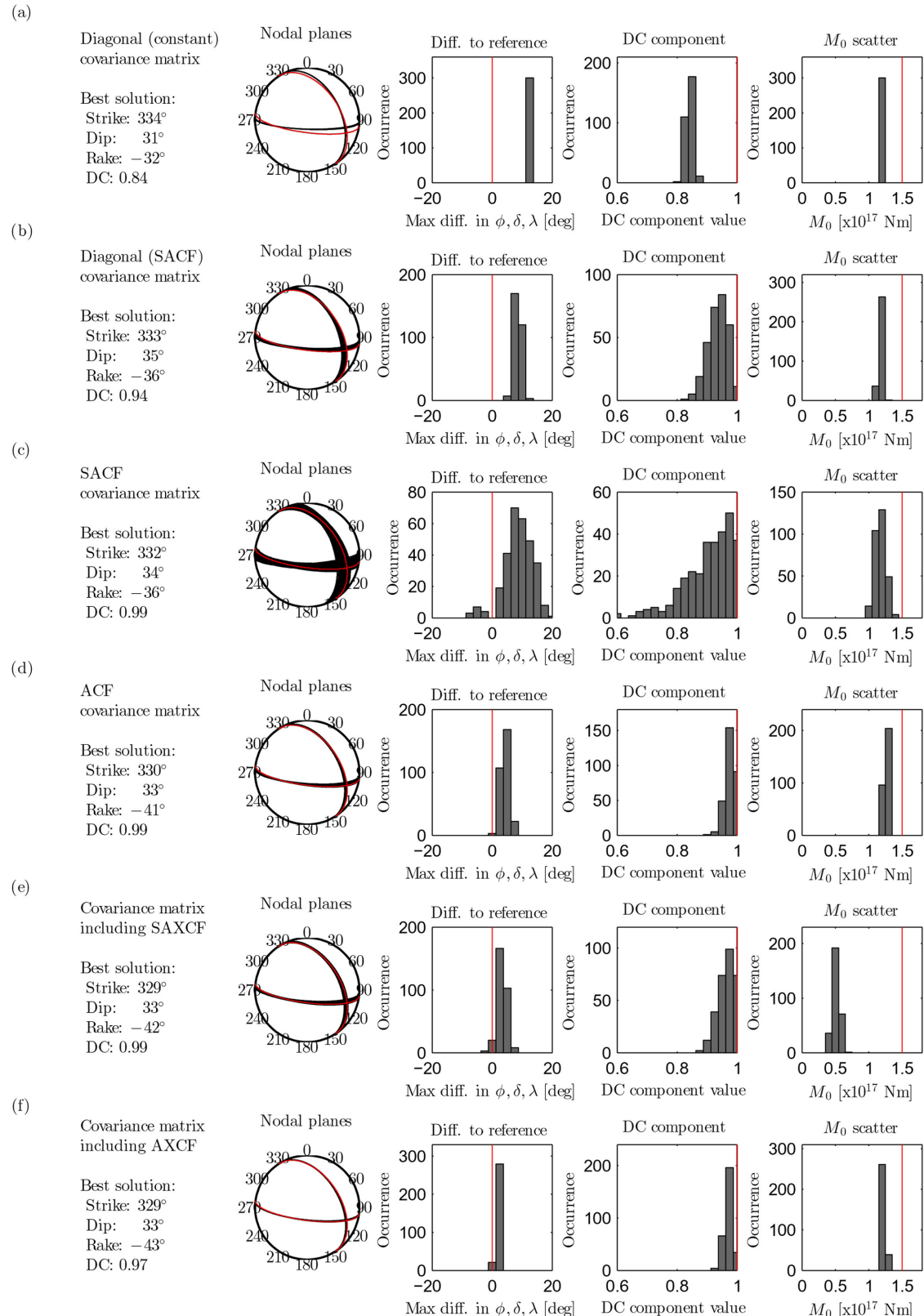


Figure 8. Result of a synthetic MT inversion test with a single realization of the randomly perturbed velocity models to generate the target data. Panels in a row are the maximum likelihood solutions (text), DC mechanism fault planes (left), maximum difference to reference in strike, dip, rake (middle-left), DC component (middle-right) and the M_0 scatter (right). Each row corresponds to the use of different type of the data covariance matrix (see legend). The beach balls and histograms are built from 300 random samples of the posterior PDF to visualize the estimated parameter uncertainty. The true solution (in red) is a pure shear mechanism (DC = 1) with strike 327°, dip 32°, rake -45°, and scalar seismic moment 1.5×10^{17} Nm.

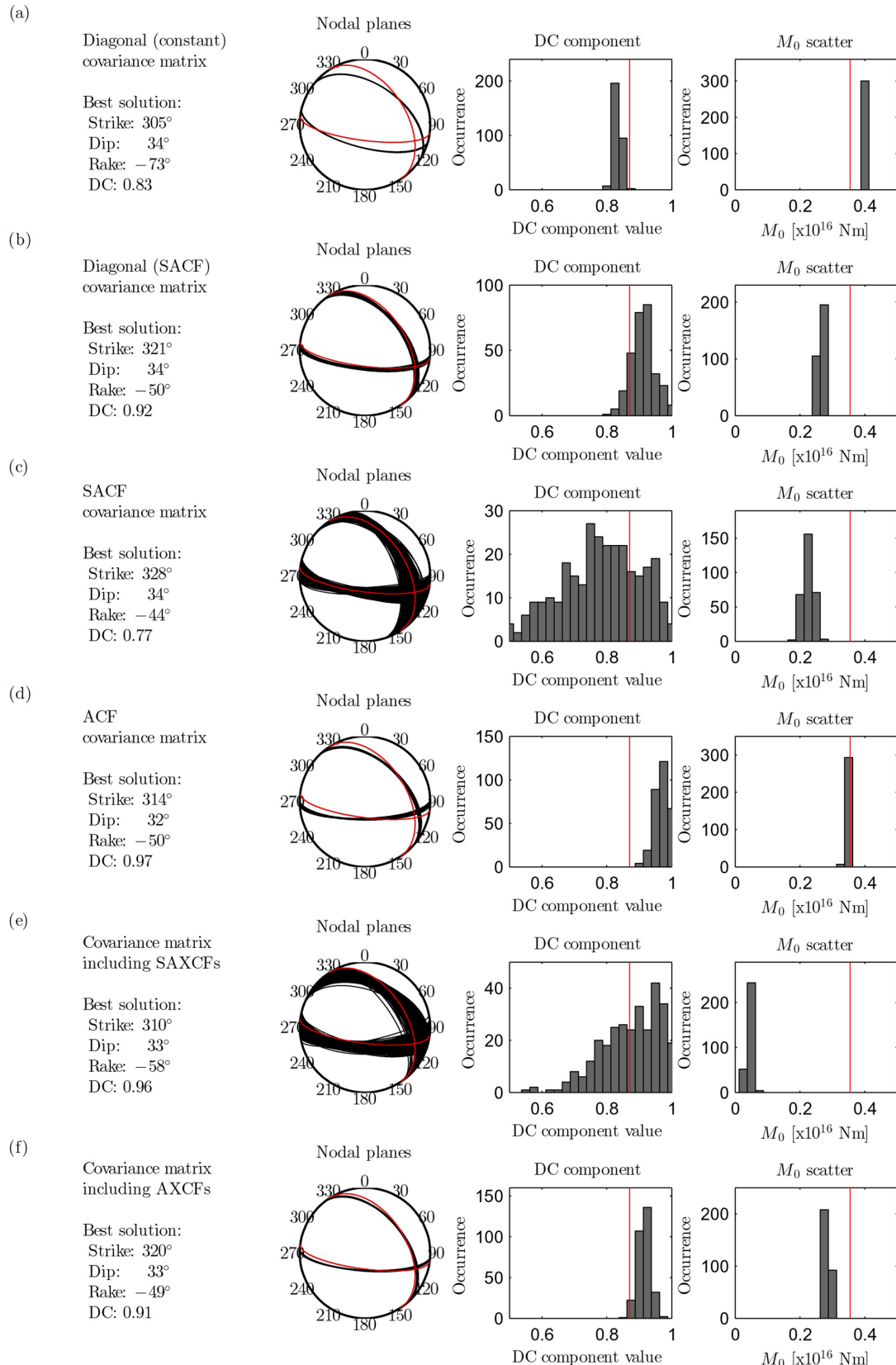


Figure 9. Same as Fig. 8 but for the real data set of the 2012 April 25 event of moment magnitude 4.3 ($M_0 = 3.55 \times 10^{15}$ Nm) from the Corinth Gulf. The reference solution by Sokos & Zahradník (2013) obtained using the same data set has strike 327°, dip 32°, rake -45° and DC component 87 per cent (in red).

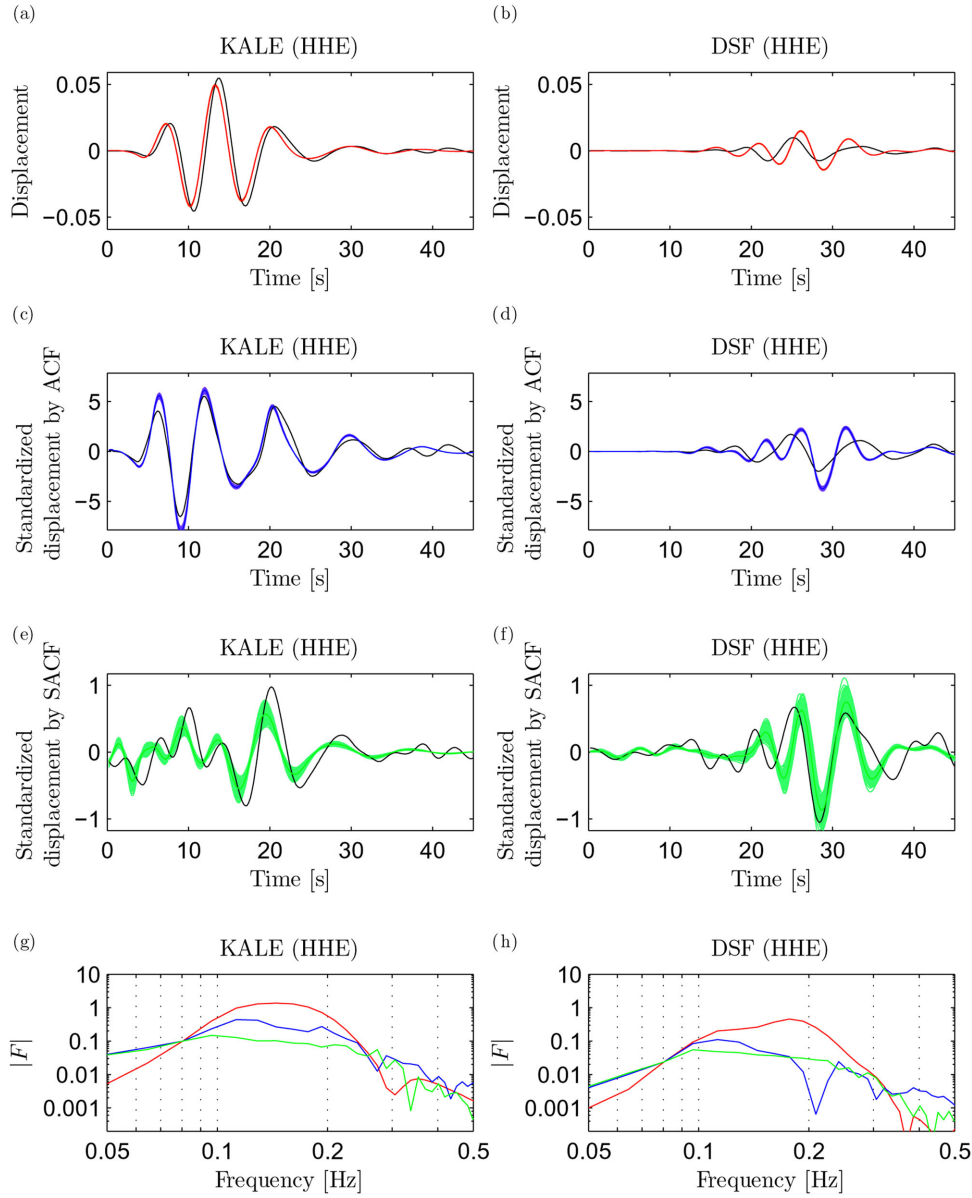


Figure 10. Standardized displacement data and synthetics at stations KALE (left) and DSF (right) for the real event of 2012 April 25 from the Corinth Gulf. Epicentral distances are 13 and 47 km for the KALE and DSF stations, respectively. Black waveforms are standardized displacements and collared waveforms are 300 realizations of the standardized synthetics perturbed by the posterior covariance matrix. Data are corrected by instrument response and bandpass Butterworth filtered between 0.1 and 0.2 Hz. Panels (a) and (b) show displacements normalized by standard deviation of the ambient noise (see the text). Data in panels (c), (d) and (e), (f) are displacements standardized by ACF and SACF covariance matrices respectively. Panels (g) and (h) show standardized amplitude spectra of the real data for diagonal (red), ACF (blue), and SACF (green) covariance matrices.

worse variance reduction for inversion with SAXCF covariance matrix correlates with the poor estimate of the scalar seismic moment in both real and synthetic tests.

3.4 Remark on the role of the covariance matrix in the inversion

As we discussed in Section 3.1, the MT inversion minimizes the difference (residuals) between the recorded data and synthetics in terms of L2 norm (eq. 19). Instead, if the covariance matrix with off-diagonal components is used, the inversion minimizes the standardized residuals, that is, waveforms multiplied by the triangular matrix from the Cholesky decomposition (see eq. 23). In Fig. 10,

we show normalized and standardized displacement fits for the real earthquake inversion. We show here data only for two selected representative stations (KALE as a close station and DSF as a distant station), for the rest of the stations see the Supporting Information.

Matrix \mathbf{R} corresponding to a diagonal covariance matrix is also diagonal, having reciprocals of square roots of the diagonal values from the \mathbf{C} matrix (i.e. reciprocals of standard deviations of the data samples). In such a case, the maximum-likelihood solution is the model that best reproduces the measured data in terms of the L2 norm of the residual seismograms weighted by the reciprocals of the data standard deviations from the \mathbf{C} matrix (see examples in Figs 10a and b). If the diagonal covariance matrix is built from the variances of the SACF covariance matrix, then the station weights

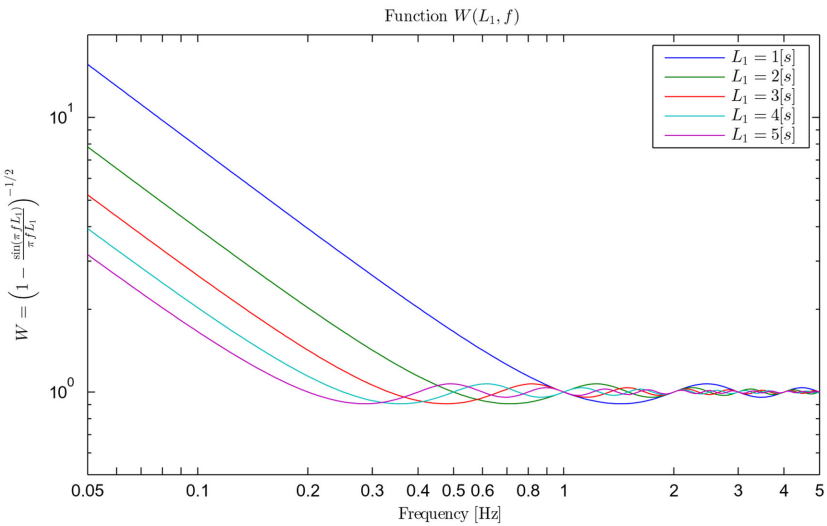


Figure 11. Implicit weighting of the signal spectral components in an inversion with SACF (see the second term in eq. 25). Colours represent various widths of the time shifts window L_1 (see legend). Note that L_1 is considered to generally increase with distance, so that the graph shows also implicit relative weighting in the spectral domain between near and distant stations.

are proportional to the signal RMS, where the constant of proportionality depends on the signal shape and considered time shifts (as illustrated in Fig. 4). Multiplying by \mathbf{R} then normalizes the waveforms to a unit RMS and amplifies the near stations with respect to the distant ones.

If the covariance matrix is constructed from a time-independent (stationarized) CF, rows of matrix \mathbf{R} are composed of all-pole (minimum-phase) IIR filters with the given CF (Marple 1986). Multiplication by \mathbf{R} in eq. (23) thus works approximately as a filter with Fourier spectrum equal to the reciprocal of the square root of Fourier spectrum of the original CF. Considering the SACF from eq. (14), such a filter has spectrum

$$\begin{aligned} W(L_1, f) &= \mathcal{F}(r_f(\tau) * (\delta(\tau) - \wedge_{2L_1}(\tau)))^{-\frac{1}{2}} \\ &= (r_f(f))^{-\frac{1}{2}} \left(1 - \frac{\sin(\pi f L_1)}{\pi f L_1}\right)^{-\frac{1}{2}}. \end{aligned} \quad (25)$$

When applied to the data vector (see examples in Figs 10e and f), the first term in eq. (25) works implicitly as data pre-whitening and normalization, that is, approximately equalizing the spectral content of the signal of all stations to a common value. The second term then implicitly amplifies the low-frequency part of the spectrum up to the reciprocal of L_1 as it is shown in Fig. 11 for various values of L_1 . Since L_1 generally increases with distance, the amplification at close stations reaches higher frequencies than at distant stations (see Fig. 11). Moreover, the closer is the station the more amplified is its spectrum in general (Fig. 11).

The pre-whitening effect and the low-frequency amplification are visible in Figs 10(g) and (h), comparing amplitude spectra of weighted real data waveforms (red) and seismograms standardized by SACF (green) for two selected stations. In particular, in case of the SACF the amplitude spectra are flat and increasing toward lower frequencies in the filter frequency range 0.1–0.2 Hz. The closer station KALE has the low-frequency part of the spectrum amplified more than the more distant station DSF (compare green lines in Figs 10g and h) due to the lower value of L_1 considered for the smaller distance.

The case when the covariance matrix is constructed from the ACF (see examples in Figs 10c and d) is more complex. Due to the

time-dependence of the ACF, it cannot be likened as an application of a time-invariant filter. However, this time-dependence is reduced when increasing L_1 , that is, as the integrals (i.e. expectations) in eq. (12) make the ACF smoother in time. In the extreme case of $L_1 \geq T$, the ACF is nearly stationary in the period of the useful signal T , and hence almost the same as the SACF tapered over the signal duration. This means that the described features of the SACF (such as equalizing the spectral content and amplifying low-frequencies) are also present in the data standardized by ACF to an extent depending on the parameter L_1 . These effects are perceptible in Figs 10(g) and (h), showing amplitude spectra of the weighted real data waveforms (red), seismograms standardized by SACF (green) and by ACF (blue), yet to lower extent than in the case of SACF. To summarize, the above interpretation of the effect of the SACF gives a hint on the implicit behaviour of the inversion when the \mathbf{C} matrix is constructed using the approximate covariances proposed in this paper.

4 SUMMARY AND CONCLUSIONS

The aim of this paper is to introduce a simple and easy-to-implement approach to efficiently involve the GF uncertainty in practical source inversions. Recent Bayesian waveform inversions rely on statistical description of the GFs uncertainty by means of a covariance matrix of a Gaussian distribution. Therefore, we introduce a fast and simple method for evaluation of the covariance matrix of GFs, incorporating uncertainty of a crustal velocity model (see eqs 11, 12, 14 and 15).

Our approximate approach requires a ‘mother’ GF and statistical description of the random time shifts of the signal as an input. While the ‘mother’ GF is calculated using a given (mean) velocity model, which is required by the source inversion anyway, the estimation of the random time shifts requires additional considerations. In particular, experiments shown in this paper suggest that it is enough to assume a uniform PDF for the time shifts. Its width L_1 depends on the source distance and velocity model perturbations linearly (Fig. 1d). In our applications, we adopt the dependence in eq. (24). Alternatively, one may estimate L_1 from temporal residuals obtained during event location, but it will require future

investigation and testing. We point out that despite the fact that the simplified formulae were derived assuming purely random time shifts of GFs, the proposed approach produces variations of both the arrival time and the waveform amplitudes as shown in Fig. 5.

An example implementation of the proposed approach is illustrated on a moment tensor inversion applied to synthetic and real data sets. Experiments with large number of synthetic target data sets obtained by randomly perturbing velocity models suggest that the lowest scatter of the maximum likelihood solutions is attained for the approximate covariance function (ACF, eq. 12), possibly in combination with the approximate cross-covariance (AXCF, eq. 11), see Fig. 7. Tests with a single realization of the target synthetics evaluated in the perturbed velocity models show that the posterior covariance matrix reflects the true uncertainty of the moment tensor inversion well when considering the stationarized auto-covariance function (SACF, eq. 14), see Fig. 8(c). Similarly, real-data inversion using the SACF (Fig. 9c) provides moment tensor uncertainty estimate comparable to the result of the jack-knifing experiment by Sokos & Zahradník (2013, fig. 3).

It is clear that the performance of the proposed approach to evaluate the GF uncertainty must undergo more thorough testing in a large number of practical applications. For easier implementation in other researchers' codes, we release open source codes for computing all the types of the proposed approximate (cross-)covariance matrices including the stationarized ones. The codes are available for downloading under GNU license on the author's website (<http://geo.mff.cuni.cz/~hallo/>) or alternatively on request by email.

ACKNOWLEDGEMENTS

We appreciate waveform data (same as in Sokos & Zahradník 2013) provided by the Hellenic Unified Seismic Network operated by the Geodynamic Institute of the National Observatory of Athens [doi:10.7914/SN/HL], the Aristotle University of Thessaloniki [doi:10.7914/SN/HT], the University of Patras [doi:10.7914/SN/HP], co-operating certain stations jointly with the Charles University in Prague, and the University of Athens. Data from station TRIZ of the Corinth Rift Laboratory Network are also greatly appreciated. We acknowledge financial support by the Czech Science Foundation project 14-04372S, the Grant Agency of the Charles University projects SVV-260218 and GAUK-728916, and Ministry of Education, Youth and Sports project LM2015079 CzechGeo/EPOS. We would like to thank Jakub Velímský for his comments on the Monte-Carlo simulations and Jiří Zahradník for inspiring comments. We are grateful to an anonymous reviewers and the editor for their comments that improved the original manuscript.

REFERENCES

- Bouchon, M., 1981. A simple method to calculate Green's functions for elastic layered media, *Bull. seism. Soc. Am.*, **71**, 959–971.
- Dettmer, J., Dosso, S.E. & Holland, C.W., 2007. Uncertainty estimation in seismo-acoustic reflection travel-time inversion, *J. acoust. Soc. Am.*, **122**, 161–176.
- Dettmer, J., Benavente, R., Cummins, P.R. & Cambridge, M., 2014. Trans-dimensional finite-fault inversion, *Geophys. J. Int.*, **199**, 735–751.
- Duputel, Z., Rivera, L., Fukahata, Y. & Kanamori, H., 2012. Uncertainty estimations for seismic source inversions, *Geophys. J. Int.*, **190**(2), 1243–1256.
- Duputel, Z., Agram, P.S., Simons, M., Minson, S.E. & Beck, J.L., 2014. Accounting for prediction uncertainty when inferring subsurface fault slip, *Geophys. J. Int.*, **197**(1), 464–482.
- Duputel, Z. *et al.*, 2015. The Iquique earthquake sequence of April 2014: Bayesian modeling accounting for prediction uncertainty, *Geophys. Res. Lett.*, **42**, 7949–7957.
- Gallovič, F. & Ampuero, J.-P., 2015. A new strategy to compare inverted rupture models exploiting the eigen-structure of the inverse problem, *Seismol. Res. Lett.*, **86**, 1679–1689.
- Gallovič, F. & Zahradník, J., 2012. Complexity of the M_w 6.3 2009 L'Aquila (Central Italy) earthquake: 1. Multiple finite-extent source inversion, *J. geophys. Res.*, **117**, B04307, doi:10.1029/2011JB008709.
- Gallovič, F., Imperatori, W. & Mai, P.M., 2015. Effects of three-dimensional crustal structure and smoothing constraint on earthquake slip inversions: case study of the M_w 6.3 2009 L'Aquila earthquake, *J. geophys. Res.*, **120**, 428–449.
- Kikuchi, M. & Kanamori, H., 1991. Inversion of complex body waves—III, *Bull. seism. Soc. Am.*, **81**(6), 2335–2350.
- Kubo, H., Asano, K., Iwata, T. & Aoi, S., 2016. Development of fully Bayesian multiple-time-window source inversion, *Geophys. J. Int.*, **204**(3), 1601–1619.
- Mai, P.M. *et al.*, 2016. The earthquake-source inversion validation (SIV) project, *Seismol. Res. Lett.*, **87**, 690–708.
- Marple, S.L., 1986. *Digital Spectral Analysis: With Applications*, Prentice-Hall, Inc.
- Minson, S.E., Simons, M. & Beck, J.L., 2013. Bayesian inversion for finite fault earthquake source models. I—Theory and algorithm, *Geophys. J. Int.*, **194**(3), 1701–1726.
- Mustać, M. & Tkalčić, H., 2016. Point source moment tensor inversion through a Bayesian hierarchical model, *Geophys. J. Int.*, **204**, 311–323.
- Piatanesi, A., Cirella, A., Spudich, P. & Cocco, M., 2007. A global search inversion for earthquake kinematic rupture history: application to the 2000 western Tottori, Japan earthquake, *J. geophys. Res.*, **112**(B7), B07314, doi:10.1029/2006JB004821.
- Sokos, E. & Zahradník, J., 2013. Evaluating centroid-moment-tensor uncertainty in the new version of ISOLA software, *Seismol. Res. Lett.*, **84**, 656–665.
- Sokos, E. *et al.*, 2015. Rupture process of the 2014 Cephalonia, Greece, earthquake doublet (M_w 6) as inferred from regional and local seismic data, *Tectonophysics*, **656**, 131–141.
- Tarantola, A., 2005. *Inverse Problem Theory and Methods for Model Parameter Estimation*, SIAM.
- Trench, W.F., 1964. An algorithm for the inversion of finite toeplitz matrices, *J. Soc. Ind. Appl. Math.*, **12**(3), 515–522.
- Vackár, J., Burjánek, J. & Zahradník, J., 2015. Automated detection of disturbances in seismic records; MouseTrap code, *Seismol. Res. Lett.*, **86**, 442–450.
- Valentine, A.P. & Trampert, J., 2012. Assessing the uncertainties on seismic source parameters: towards realistic error estimates for centroid-moment-tensor determinations, *Phys. Earth planet. Inter.*, **210–211**, 36–49.
- Valentine, A.P. & Woodhouse, J.H., 2010. Approaches to automated data selection for global seismic tomography, *Geophys. J. Int.*, **182**(2), 1001–1012.
- Yagi, Y. & Fukahata, Y., 2011. Introduction of uncertainty of Green's function into waveform inversion for seismic source processes, *Geophys. J. Int.*, **186**(2), 711–720.
- Zahradník, J. & Plešinger, A., 2010. Toward understanding subtle instrumentation effects associated with weak seismic events in the near field, *Bull. seism. Soc. Am.*, **100**, 59–73.
- Zahradník, J. & Custódio, S., 2012. Moment tensor resolvability: application to Southwest Iberia, *Bull. seism. Soc. Am.*, **102**, 1235–1254.
- Zahradník, J., Fojtíková, L., Carvalho, J., Barros, L.V., Sokos, E. & Janský, J., 2015. Compromising polarity and waveform constraints in focal-mechanism solutions; the Mara Rosa 2010 M_w 4 central Brazil earthquake revisited, *J. South Am. Earth Sci.*, **63**, 323–333.

SUPPORTING INFORMATION

Additional Supporting Information may be found in the online version of this article:

SUPPLEMENT A: Derivation of stationarized approximate covariance functions (SACF and SAXCF)

SUPPLEMENT B: Example of cross-covariance of two nearby receivers

Figure B1. An example of the cross-covariance for two nearby receivers. Panels (a) and (b) show two sets of GFs for the source-receiver distances 50 and 60 km, respectively, computed by the discrete wavenumber method ($\sigma_M = 10$ per cent). The black lines are the mother GFs calculated in the mean velocity model. Other colours of waveforms have no meaning and are used only for clearer view. Panel (c) shows full cross-covariance matrices for velocity model perturbations ($\sigma_M = 10$ per cent), as obtained by the Monte-Carlo approach, while matrices in panels (d) and (e) were obtained by the approximate formulae in eqs (11) and (15), respectively. Duration of the dominant part of the earthquake signal was set up as $T = 15[s]$. Finally, panel (f) shows comparison of stationarized Monte-Carlo cross-covariance function (black) and SAXCF obtained using eq. (15) (red).

Figure B2. Distributions of time shifts of GFs due to velocity model perturbations for the example in Fig. B1. Time shifts are estimated from waveforms filtered at very low frequencies (0.05–0.09 Hz) to avoid cycle skipping. The red lines show the characteristic widths of the time shift distributions ($4\sigma_t$): (a) Joint time shifts, $4\sigma_t = 1.86[s]$; (b) relative (interstation) time shifts, $4\sigma_t = 0.49[s]$.

SUPPLEMENT C: Examples of complete covariance matrices used in the source inversion

Figure C1. Synthetic waveforms on the DSF station for the synthetic inversion test described in the main text. Data are filtered by Butterworth bandpass filter between 0.1 and 0.2 Hz.

Figure C2. Submatrices for the six different types of covariance matrices discussed in the main text (see titles in figure) corresponding to the DSF station. There are shown three blocks of auto-covariances and six blocks of cross-covariances among DSF station's components in each submatrix. The values shown by colour have units [mm^2].

SUPPLEMENT D: Fit of the standardized waveforms for the real data inversion example

Figure D1. Normalized displacement (black) and synthetic (colour) disregarding uncertainty of GFs. Data are corrected by instrument response and filtered by Butterworth bandpass filter between 0.1 and 0.2 Hz. Black waveforms are normalized displacement and coloured waveforms are 300 synthetic realizations of normalized displacement perturbed around the best-fitting solution by posteriori covariance.

Figure D2. Same as Fig. D1, but for standardized displacement and synthetic realizations considering uncertainty of GFs by means of ACF.

Figure D3. Same as Fig. D1, but for standardized displacement and synthetic realizations considering uncertainty of GFs by means of SACF (<http://gji.oxfordjournals.org/lookup/suppl/doi:10.1093/gji/ggw320/-DC1>).

Please note: Oxford University Press is not responsible for the content or functionality of any supporting materials supplied by the authors. Any queries (other than missing material) should be directed to the corresponding author for the paper.

APPENDIX A: EXAMPLE OF APPROXIMATED CROSS-COVARIANCE FOR STATION COMPONENTS

Here we show an example of performance of the approximated cross-covariances in reproducing those obtained by the Monte-Carlo simulations using methodology analogical to that described in the main text. We use the same 1500 randomly perturbed velocity models with $\sigma_M = 10$ per cent (see Fig. 1a). Fig. A1 shows examples of the resulting synthetic waveforms at two components of a single receiver.

In this particular case, the two ‘mother’ waveforms $f(t)$ and $g(t)$ share the joint time shift distribution ($L_1 > 0$) with no relative random time shift between the two components ($L_{12} = 0$). The ‘mother’ waveforms for the two components (evaluated in the mean velocity model) are shown in black in Figs A1(a) and (b). Cross-covariance matrix estimated using the ensemble of the waveforms (eq. 1) is shown in Fig. A1(c). Note that, contrarily to the auto-covariance, the cross-covariance is not symmetrical around the diagonal. Fig. A1(d) displays the approximated cross-covariance matrix (AXCF) obtained using eq. (11). There is some difference between the Monte-Carlo XCF and AXCF cross-covariance matrices, but they are close in terms of their patterns including signs. Finally, stationarized Monte-Carlo and approximate (SAXCF) cross-covariances, compared in Fig. A1(f), agree very well.

The AXCF (or SAXCF) cross-covariance could be in principle computed for any arbitrary GF components of different stations, until they share a common random time shift ($L_1 > 0$). This joint time shift requires alike wave propagation along at least a part of the path between the source and the receivers, such as for two nearby receivers ($L_1 > L_{12} > 0$). We show an example of the cross-covariance for such two nearby receivers (source–receiver distances 50 and 60 km) in the Supporting Information.

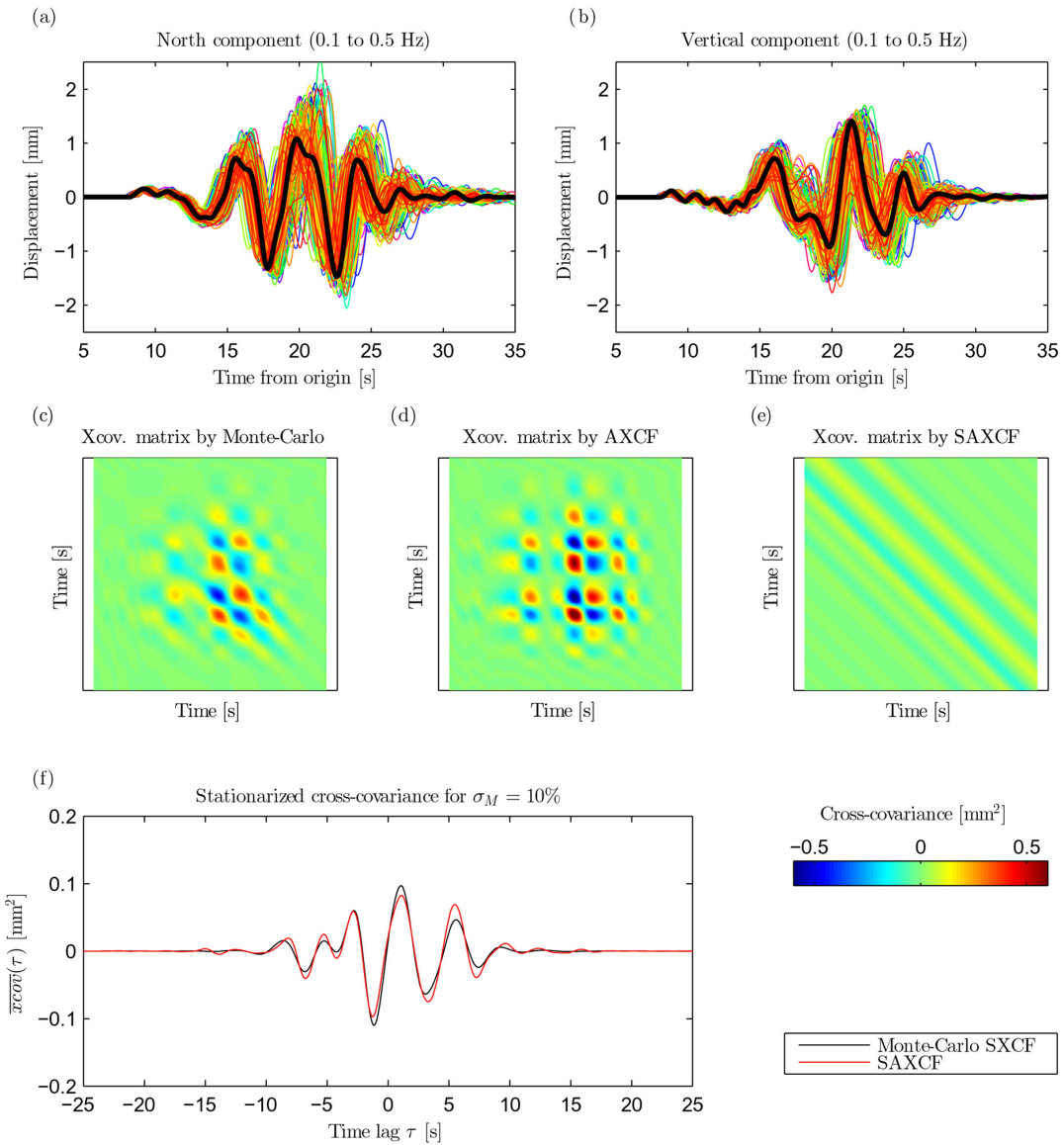


Figure A1. Examples of the cross-covariance for two components at a receiver. Panels (a) and (b) show two sets of GFs for the North and vertical component, respectively, computed by the discrete wavenumber method for the source–receiver distance of 50 km ($\sigma_M = 10$ per cent). The black lines are the ‘mother’ GFs calculated in the mean velocity model. Other colours of waveforms have no meaning and are used only for clearer view. Panel (c) shows cross-covariance matrices for velocity model perturbations ($\sigma_M = 10$ per cent) as obtained by the Monte-Carlo approach, while matrices in panels (d) and (e) were obtained by the approximate formulae in eqs (11) and (15), respectively. The width of the uniform PDF $L_1 = 4\sigma_t$, used in the approximate formulae is adopted from graph in Fig. 1(d); L_{12} is set to zero as the velocity model is the same for the both components. Duration of the dominant part of the earthquake signal was set $T = 15$ sec. Panel (f) shows comparison of the stationarized Monte-Carlo cross-covariance function (black) and the SAXCF obtained using eq. (15) (red).

APPENDIX B: LIST OF USED ABBREVIATIONS

Auto-covariance related:

- CF—auto-covariance function— $\text{cov}(t, \tau)$ —eq. (2)
- ACF—approximate auto-covariance function— $\widetilde{\text{cov}}(t, \tau)$ —eq. (12)
- SCF—stationarized auto-covariance function
- SACF—stationarized approximate auto-covariance function— $\overline{\text{cov}}(\tau)$ —eq. (14)

Cross-covariance related:

- XCF—cross-covariance function— $x\text{cov}(t, \tau)$ —eq. (1)

AXCF—approximate cross-covariance function— $\widetilde{x\text{cov}}(t, \tau)$ —eq. (11)

SXCF—stationarized cross-covariance function

SACF—stationarized approximate cross-covariance function— $\overline{x\text{cov}}(\tau)$ —eq. (15)

Others:

DC—double-couple

GF—Green’s function

MT—moment tensor

PDF—probability density function

RMS—root-mean-square